Interaction between an elliptic vortex ring and a bubble: effect of capture angle

MANOJ N DIXIT and RAGHURAMAN N GOVARDHAN*

Department of Mechanical Engineering, Indian Institute of Science, Bengaluru, Karnataka, India
e-mail: rng@iisc.ac.in

Abstract. The rich interaction of multiple bubbles with multiple vortical structures makes the study of bubbly turbulent flows quite challenging. An idealisation of this problem would be the interaction between a single bubble and an elliptic vortex ring, the latter of which can be considered a representative vortical structure. The elliptic vortex ring is characterised by its initial aspect ratio AR_0, defined as the ratio of the semi-minor to semi-major axes of the ellipse, with $AR_0 = 1$ corresponding to a circular vortex ring. In the first part, we focus on the interaction between the elliptic vortex ring ($AR_0 = 0.6$) and a bubble, where we explore the effects of the capture angle (θ_C) on the different quantities relevant to the ring as well as the bubble, using simultaneous side and top-view high-speed visualisations; θ_C is defined as the angle subtended by the bubble with the instantaneous major axis of the elliptic vortex ring at bubble capture. We study the effect of θ_C on the reduction in the ring's convection speed ΔU^* and the number of daughter bubbles N_b, computed at a later stage of the interaction. For this part of the study, the Weber number $We = \rho U_0^2 D_b / \sigma$, defined as the ratio of the ring's inertial effects to surface tension effects, is fixed at $We = 11$. We find that bubble capture at lower capture angles ($\theta_C \approx 0°$) corresponding to the high-curvature part of the elliptic vortex ring is found to be more probable compared to that at higher capture angles ($\theta_C \approx 90°$). Further, a lower capture angle ($\theta_C \approx 0°$) leads to a larger number of daughter bubbles N_b and a slightly higher reduction in ring speed ΔU^*. In the second part, we study the effect of AR_0 by contrasting the elliptic ring ($AR_0 = 0.6$) with a circular ring ($AR_0 = 1$) over a range of Weber numbers, in which the parameters of interest are the ring's speed and the number of daughter bubbles. We observe that the elliptic vortex ring produces fewer daughter bubbles than the circular ring, with the difference increasing at larger ring strengths corresponding to higher Weber numbers. At higher We, the elliptic ring deviates from the $N_b \propto We^{0.42}$ scaling, which holds for the circular ring. The current study thus helps to gain a better insight into the complex problem of bubbly turbulent flows.

Keywords. Elliptic vortex ring; Bubble; Bubbly turbulent flow.

1. Introduction

Bubbly turbulent flows are found in many situations like ship hydrodynamics, oil transportation, and chemical/nuclear reactors, in addition to natural flow settings like air bubbles in the upper ocean or vapour bubbles in geysers [1]. In these flows, the bubbles exhibit motion and deformation when they interact with the turbulent boundary layer and lead to the modulation of the turbulence. The dispersed phase can influence the transport of mass, momentum and energy transport across the carrier and the dispersed phases [2, 3]. However, as discussed in the review article [4], the mechanisms through which the dispersed phase modifies the turbulence and the parametric dependence are poorly understood, making the topic wide open for fundamental investigation. Turbulent boundary layers are characterised by hairpin-shaped vortical structures [5] (also called eddies) that play a fundamental role in governing the flow dynamics. Therefore, bubbly turbulent flow can be interpreted as the interaction between multiple bubbles and multiple eddies. However, due to the high number density, multi-scale nature, and unsteadiness of the hairpin vortices, measurements on individual vortices are challenging, and the dispersed phase makes them more formidable. Therefore, a simplification of the complex problem would be the interaction between an elliptic vortex ring and a bubble, where the elliptic vortex ring is an idealistic representation of a vortical structure. The elliptic ring serves as a more general representation of the hairpin structures owing to its dynamic nature compared to the circular ring. The circular ring is a subset of the more general class of elliptic rings.
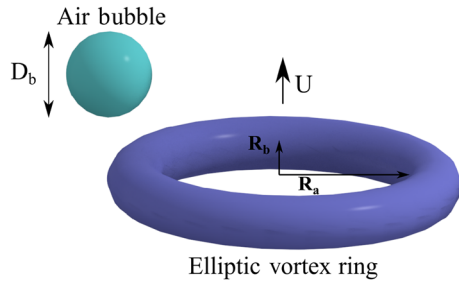
Figure 1. Schematic of the interaction between an elliptic vortex ring and a bubble. The elliptic vortex ring is characterized by the aspect ratio $AR_0 = R_b/R_a$, where R_b and R_a are, respectively, the semi-minor and semi-major axes of the ellipse defining the vortex ring. $AR_0 = 1$ refers to the circular vortex ring.

Bubble injection in turbulent flows has many applications, like drag reduction in marine vehicles. One mechanism for the reduction of skin-friction drag by bubbles is the disruption of these vortical structures in the turbulent boundary layers [6]. Given the complexity of such interactions, we are interested in studying how a single bubble disrupts the vortex ring as an idealised case. However, few studies can be found on the interaction between a bubble and a circular vortex ring. Sridhar and Katz [7] experimentally studied how small bubbles affect the structure of a vortex ring. They observed vortex core distortion by the bubbles for a small volume ratio, defined as the ratio of the total bubble volume to the vortex ring core volume ($V_R \approx 10^{-6}$). Jha and Govardhan [8], in their experimental work, investigated the effects of the Weber number in ring-bubble interactions and observed ring core fragmentation followed by a reduction in the ring's enstrophy at large volume ratio ($V_R \approx 0.1$). Biswas and Govardhan [9] have observed similar trends in the case of two bubbles and many bubbles interacting with a vortex ring. In another recent study [10], the authors have studied the effect of bubble-to-vortex size ratio on the bubble and ring dynamics during the interaction of a single bubble with a single vortex ring, where they find that increasing the bubble size leads to an increase in the ring disruption, with these effects being significant at low Weber numbers. However, not many studies have been done on the influence of the vortex ring curvature on the interaction between a vortex ring and a bubble. One way to explore this is to consider an elliptic vortex ring, where the local vortex curvature varies [11], as in the case of hairpin structures in the turbulent boundary layer. This motivates us to consider the interaction between an elliptic vortex ring and a bubble.

The variation in the local curvature of the elliptic vortex ring leads to a variation in the local induced velocity, which causes an oscillatory, 3D spatial deformation of the ring leading to the well-known axis-switching phenomenon [12]. The dynamics of the elliptic ring is a function of the ring's initial aspect ratio $AR_0 = R_b/R_a$, where R_b and R_a are, respectively, the semi-minor and semi-major axis

lengths of the ellipse defining the ring's elliptical toroidal axis. While the elliptic ring exhibits axis-switching for moderate departures of AR_0 from unity, at higher departures, it undergoes a partial or complete bifurcation due to cross-linking of vorticity to yield two or three sub-rings [13]. The oscillatory deformation of the elliptic ring plays a vital role in the mass entrainment and mixing enhancement [14]. The elliptic vortex ring thus offers rich dynamics which could be related to the behaviour of the hairpin-shaped vortical structures in the turbulent boundary layer. It could therefore be employed in studying the simplified problem of the interaction between a vortex ring and a bubble. However, to the authors' knowledge, not many studies are trying to understand the role of vortex curvature in the interaction of vortex rings with bubble(s). We thus explore the influence of the vortex ring curvature, which we quantify by the ring's initial aspect ratio AR_0, on the interaction between a vortex ring and a bubble, as shown in the schematic in figure 1. We are interested here in both the effect of the ring on the bubble in terms of the bubble dynamics and the effect of the bubble on the ring in terms of the ring dynamics.

2. Methodology

The experiments are carried out in a glass tank of capacity $0.6 \times 0.6 \times 1$ m^3, with transparent side walls for optical access, as shown in figure 2. Using a piston-cylinder arrangement, a vortex ring is generated by imparting an impulse to a fluid mass out of a circular/elliptic nozzle of diameter D_n. For the elliptic nozzle, D_n is the diameter of the area-equivalent circle. The vortex ring has a radius R (the area-equivalent radius for the elliptic ring) and a core radius r_C and travels upwards (along the z-direction) against gravity. The piston is given an impulsive velocity profile using a known impulse I. By varying I, we achieve a wide range of the ring's initial convection speed U_0. The core of the vortex ring is identified by introducing micron-sized bubbles generated by electrolysis at the tip of the circular/elliptic nozzle, which are entrained into the core owing to the core's low pressure. These microbubbles are much smaller (average diameter 400 μm) compared to the main bubble (diameter $D_b = 5$ mm) and hence are expected to have a negligible impact on the broad characteristics of the ring [15]. The ratio of piston stroke length to generator diameter is kept at less than 4 to inhibit the trailing jet behind the vortex ring [12]. As the bubble is released closer to the ring's core, it is captured by the low-pressure core, and the interaction between the ring and the bubble begins.

Table 1 shows the parameters used in the current study. The elliptic vortex ring is characterised by its initial convection speed U_0, and the initial aspect ratio $AR_0 = R_b/R_a$, where R_b and R_a are respectively the semi-minor and semi-major axes of the elliptic vortex ring. The non-dimensional
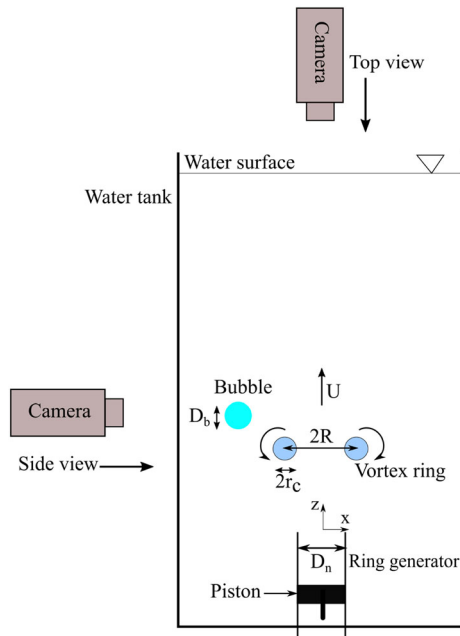
Figure 2. Schematic of the experimental setup used. The vortex ring, which is generated by giving an impulse to a fluid mass out of the circular/elliptic nozzle (ring generator) of diameter D_n, travels upwards (along the z-direction) with a convection speed U due to the upward direction of the impulse. For the elliptic nozzle, D_n is the diameter of the area-equivalent circle. The ring has a radius R and a core radius r_C. The bubble, released close to the vortex ring, has a diameter of D_b and rises upwards due to buoyancy. Side and top visualisations are done using high-speed cameras to capture the interaction.

core radius ($\epsilon = r_C/R$) is maintained at about 0.2 such that the vortex ring is thin [16]. Further, two parameters are obtained from the experiments – capture angle θ_C, defined in figure 4(d), as the angle subtended by the bubble with the instantaneous major axis of the elliptic vortex ring at bubble capture, and AR_C, the instantaneous aspect ratio of the ring at bubble capture. It is to be recalled that the elliptic ring undergoes axis switching so that the instantaneous aspect ratio varies periodically with time between the values AR_0 and unity [11]. Therefore, AR_C is found to vary across different experimental runs, depending upon the time instant at which the bubble is captured. For the current study, $AR_0 = 0.6, 1$ are chosen, where the case $AR_0 = 1$ represents the circular vortex ring as a special case of the elliptic ring. The vortex ring's effective radius $R = \sqrt{R_a R_b}$ is defined based on the area-equivalent circle for the ellipse and is maintained the same for both the AR_0 cases studied. In a bubbly turbulent flow, hairpin vortices of various aspect ratios could be present. However, we note that for $AR_0 \ll 1$, the base (non-interacting) elliptic vortex ring exhibits numerous phenomena like partial bifurcation, vorticity cancellation due to touching of cores, or complete bifurcation [13], due to which the probability of the bubble-ring interaction is very less. On the other hand, an elliptic
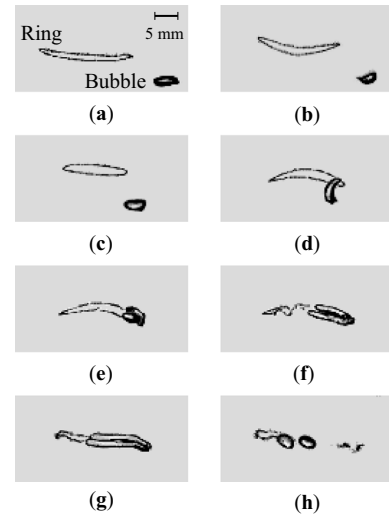
Figure 3. Side-view high-speed shadowgraphy images of the stages in the interaction between an elliptic vortex ring and a bubble: (a)–(c) before capture; the ring's axis switch is evident, (d)–(e) capture, (f)–(g) bubble elongation, (h) breakup into daughter bubbles. The ring's toroidal axis is marked by tiny microbubbles generated by electrolysis. Time stamps: $t/t_p \approx 0, 0.5, 1, 1.25, 1.5, 1.75, 2, 6$, where t_p is the axis switch time period of the base (non-interacting) elliptic vortex ring. In this case, $We = 11$. The length scale of the images is mentioned in (a).

Table 1. List of non-dimensional parameters relevant to the problem.

Parameters	Range
$AR_0 = R_b/R_a$	0.6, 1
$\epsilon = r_C/R$	0.2
$We = \rho U_0^2 D_b/\sigma$	3–166
$V_R = (\pi D_b^3/6)/(2\pi^2 r_C^2 R)$	0.08
$D_b/2r_C$	1.0
AR_C	0.6–1
θ_C	0°–90°

vortex ring with AR_0 closer to unity is not expected to show significant differences as compared to the circular ring. Hence, the value chosen for the elliptic vortex ring in this study $AR_0 = 0.6$ is a reasonable one. The Weber number, defined as $We = \rho U_0^2 D_b/\sigma$, is around 11 for the first part of the study and takes values from about 3 to 166 in the second part. Here, ρ and σ are the density of water and surface tension at the air-water interface, and D_b is the bubble diameter. The volume ratio $V_R = (\pi D_b^3/6)/(2\pi^2 r_C^2 R)$ is the ratio of bubble volume to vortex ring volume and is kept to nearly 0.08. This corresponds to $D_b/2r_C \approx 1$, which is representative of the ratio of length scales of the bubble and the ring. We note in passing that all the parameters in Table 1 except θ_C and AR_C are control parameters; θ_C and

AR_C are capture-related parameters that cannot be directly controlled.

We obtain information on the vortex ring's vertical position (z) with time (t) using side-view high-speed shadowgraphy. Additionally, we capture the bubble dynamics and measure the capture angle (θ_C) from top-view high-speed visualisation. The slope of the z-t curve gives the ring's convection speed U_{base} and $U_{interaction}$, respectively, for the base (no bubble) and interaction (with bubble) cases. Two Phantom Miro M110 high-speed cameras were used for this purpose and were triggered simultaneously using a function generator. Simultaneous side and top-view measurements enable us to correlate the parameters AR_C and θ_C to the output parameters, namely, the ring speed reduction $\Delta U^*(\%) = 100 \times (1 - U_{interaction}/U_{base})$, computed at a later time after bubble capture.
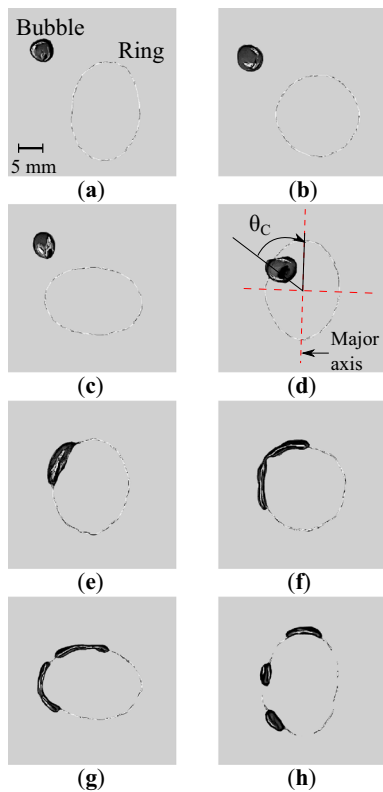
Figure 4. Top-view high-speed images of the stages in the interaction between an elliptic vortex ring and a bubble: (a)–(c) before capture; the ring's axis switch is evident, (d)–(e) capture, (f)–(g) bubble elongation, (h) breakup into daughter bubbles. The ring's toroidal axis is marked by tiny microbubbles generated by electrolysis. The time stamps are kept broadly the same as in figure 3. In (d), the capture angle θ_C is defined as the angle subtended by the bubble with the instantaneous major axis (marked by a small black arrow) of the elliptic vortex ring during capture. In this case, $We = 11$.

3. Results and discussion

We present the results in two parts. Firstly, we look at the interaction of an elliptic vortex ring with a single bubble, where we explore the effect of capture angle on the ring and bubble dynamics. Here, the Weber number denoting the ratio of the ring's inertial effects to surface tension effects is kept at $We = 11$. In the second part, we discuss the effect of the vortex ring's initial aspect ratio on the interaction by contrasting an elliptic vortex ring with a circular vortex ring for a range of Weber numbers.

3.1 *Elliptic ring-bubble interaction*

We begin by looking at the different stages of the interaction between the elliptic vortex ring and the bubble. The visualisation and results presented in this subsection correspond to $We = 11$. As in the shadowgraphy images of figure 3(a) and top-view images of figure 4(a), the ring is marked by micron-sized electrolysis bubbles before the capture of the main bubble. In figures 3(a–c) and 4(a–c), the axis switching of the ring is evident. Due to the low pressure in the vortex core, the buoyant air bubble is entrained into the ring as it approaches the latter, as in figures 3(d) and 4(d). At this stage, we define the capture angle θ_C, in figure 4(d), as the angle subtended by the bubble with the instantaneous major axis of the elliptic ring at capture. Note that the instantaneous ring aspect ratio at capture AR_C also varies across experimental runs. The entrained bubble is then elongated due to the azimuthal pressure differences along the vortex core [8], as shown in figures 3(e–g) and 4(e–g). After a sufficiently long time, the elongated bubble undergoes a Rayleigh-Plateau type of instability [8] to finally break into many daughter bubbles. The time stamps shown in the figures give us a broad perspective on the time scale of the events relative to the axis-switching time period. These stages of the interaction of the elliptic ring with the bubble are broadly similar to those of the circular ring [9, 10, 15], in which the axis-switching is absent. The main qualitative differences between $AR_0 = 0.6$ and $AR_0 = 1$ are the importance of θ_C and AR_C and the ring's continued axis switching during the interaction. AR_C can take values between AR_0 and unity. We now explore in detail the interaction between the elliptic vortex ring and the bubble.

As we see in figure 4(h), the bubble breaks into a number of daughter bubbles during the interaction. We are thus interested in examining the effect of capture angle (θ_C) on the final number of daughter bubbles (N_b). To begin with, in figure 6, we plot the histogram of the capture angle using 55 independent experimental runs, in which only θ_C and AR_C are allowed to vary. It may be observed that there is a higher probability near $\theta_C \approx 0°$ as compared to $\theta_C \approx 90°$. One should note that $\theta_C = 0°$ corresponds to the high-curvature region of the elliptic vortex ring, while $\theta_C = 90°$ corresponds to the low-curvature region of the vortex ring.

$\theta_C \approx 0°$　　$\theta_C \approx 90°$
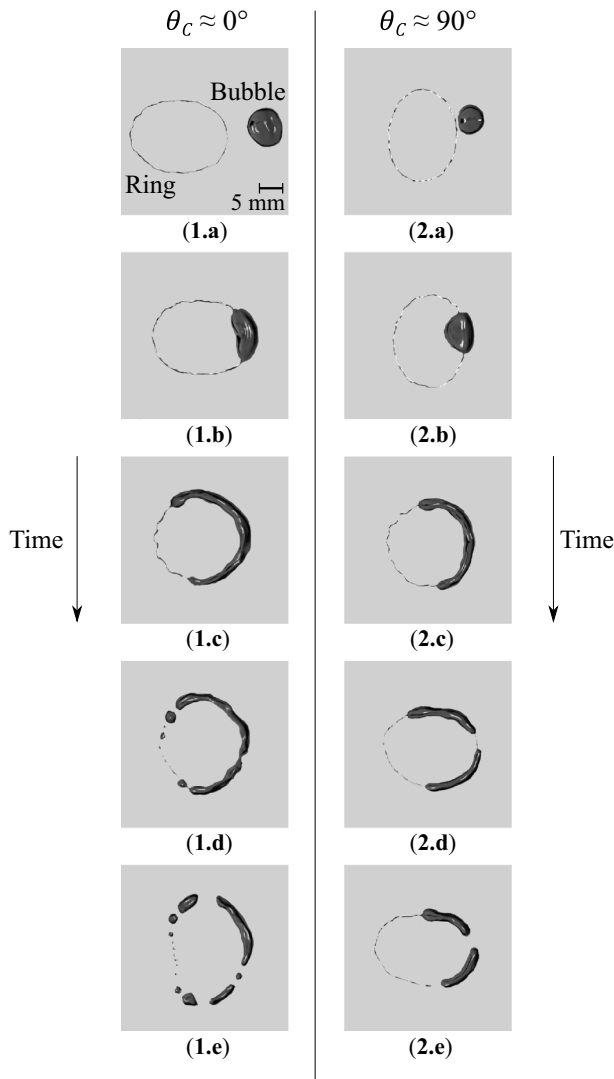
Figure 5. Top-view high-speed images of the stages in the capture process of the bubble into the elliptic vortex ring for different capture angles: (1.a)–(1.e) correspond to $\theta_C \approx 0°$, while (2.a)–(2.e) correspond to $\theta_C \approx 90°$. (1.a), (2.a): before capture. (1.b), (2.b): bubble capture completed. (1.c), (2.c): $AR(t) \approx 1$ due to axis switching. (1.d): elongated bubble first breaks at its ends. (2.d): elongated bubble first breaks at its middle portion. (1.e): the slender bubble in the middle further breaks, producing 5 to 6 daughter bubbles. (2.e): the two relatively shorter bubbles undergo no further breakup, leading to 2 or 3 daughter bubbles. Time stamps are respectively $t/t_p \approx 0, 0.5, 0.8, 1.0, 1.6$, where t_p is the axis switch time period of the base (non-interacting) elliptic vortex ring.

It is known that the induced velocity is directly proportional to the vortex curvature [11] and is thus higher at $\theta_C = 0°$. Although the complete reason for the higher probability of capture at $\theta_C \approx 0°$ is not known, we speculate that it could be because of the pressure being lower at the high-curvature region in the vortex core than at the low-curvature region, so that the pressure difference between the ambient and

vortex core would be higher at $\theta_C = 0°$ than at $\theta_C = 90°$. This higher pressure difference could lead to the higher probability of the bubble entrained at $\theta_C \approx 0°$ than at $\theta_C \approx 90°$. In a bubbly turbulent flow configuration, this could imply that the bubbles most probably interact with highly curved portions of the vortical structures, such as in the hairpin structures present in the boundary layer.
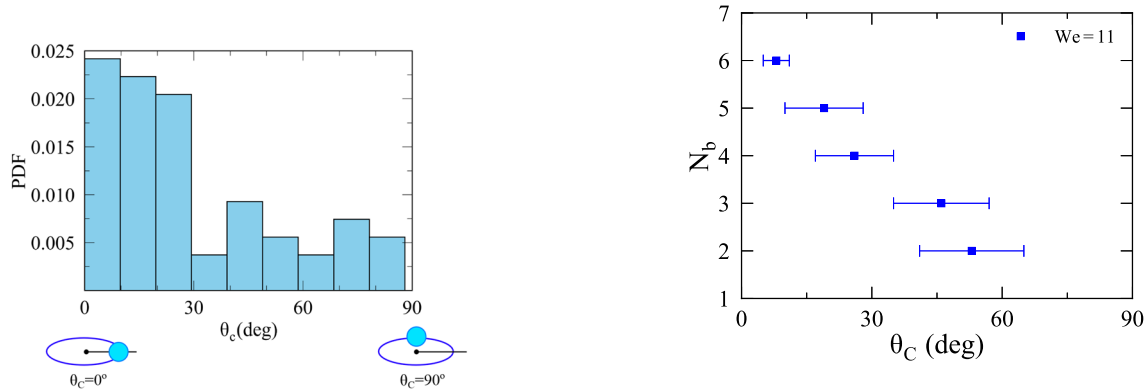
We now look at the effect of θ_C on the final number of daughter bubbles (N_b), plotted in figure 7. Although one could plot the variation of N_b over different experimental runs for different intervals of θ_C, we choose to plot the variation in θ_C for each value of N_b since N_b is better understood as a whole number. The number of daughter bubbles (N_b) monotonically increases with decreasing θ_C. This means that bubble capture at the high-curvature regions ($\theta_C \approx 0°$) leads to a larger number of daughter bubbles compared to bubble capture at the low-curvature regions ($\theta_C \approx 90°$). To understand the processes that lead to this result, in figure 5, we look at the top-view images of the capture process in detail. We contrast the extreme cases of $\theta_C \approx 0°$ in the left column (labelled (1.a)–(1.e)) with $\theta_C \approx 90°$ in the right column (labelled (2.a)–(2.e)). The time (t) is normalised by the axis switching time period (t_p) of the base (non-interacting) elliptic vortex ring. The capture time is defined as the time taken by the bubble to reach the core centre (figures 5(1.b) and 5(2.b)) from a distance $\approx 3r_C$ (figures 5(1.a) and 5(2.a)), on the lines of [15]. The capture time is thus about 0.5 times the axis switch time period as seen from the time stamps. With time, the bubble undergoes elongation, while the elliptic vortex ring continues to switch its axis and its instantaneous aspect ratio reaches nearly unity at $t/t_p \approx 0.8$ (figures 5(1.c) and 5(2.c)). After this stage, we begin to see a difference in the bubble-ring configurations for $\theta_C \approx 0°$ and $\theta_C \approx 90°$. At $t/t_p \approx 1$, in the case of $\theta_C \approx 0°$, the ends of the elongated bubble are exposed to the high-curvature ends of the ring, which give rise to small daughter bubbles and a long slender bubble, as in figure 5(1.d). On the other hand, in the case of $\theta_C \approx 90°$, we observe that the middle portion of the elongated bubble is exposed to the high-curvature region of the ring, due to which it breaks at the middle, producing two daughter bubbles of shorter but nearly equal length, as shown in figure 5(2.d). The long slender bubble in figure 5(1.d) further undergoes instability and breaks up producing 5 to 6 bubbles, as also seen in [15, 17]. On the other hand, the breakup of the relatively shorter bubbles in figure 5(2.d) is discouraged to finally produce 2 or 3 bubbles, similar to binary or tertiary breakup observed in [18]. Another interesting observation is the effect of bubble capture and elongation on the ring's axis switching, quantified by the axis switching period t_p, defined as the time taken by the base (non-interacting) elliptic vortex ring to start from $AR(t) = AR_0$, pass through $AR(t) = 1$, and reach back $AR(t) = AR_0$. During the interaction, however, it can be seen from the visualisation and time stamps in

figures 5(1.e) and 5(2.e), that the time taken to complete one axis switch is $t/t_p \approx 1.6$, which is nearly 60% higher than that of the base (non-interacting) ring. Therefore, it is evident that the processes of bubble capture and elongation delay the axis switching time period of the elliptic vortex ring.

Next, we ask the question as to how the ring's dynamics, characterised by its convection speed, change with θ_C. As mentioned in §2, we obtain the ring's vertical position (z/R) with time (tU_0/R) from high-speed visualisations, as plotted in figure 8 for the base and the interaction cases. Here, the position (z) is normalised by the ring radius (R) and the time (t) is normalised by the convective time scale of the ring (R/U_0). Here, R is the radius of the area-equivalent circle for the ellipse. The interaction case shown corresponds to $AR_C = 0.7$ and $\theta_C = 35°$, where the bubble capture has occurred at $tU_0/R \approx 13$. As discussed in §2, the slope of the curve gives the ring's convection speed U_{base} and $U_{interaction}$ respectively for the base (no bubble) and interaction (with bubble) cases. We define the reduction in the speed of the ring as $\Delta U^* \, (\%) = 100 \times (1 - U_{interaction}/U_{base})$, where the speeds are computed at a later time after bubble capture ($tU_0/R \approx 29$ for the case shown in figure 8). As AR_C and θ_C vary across experimental runs, we first present a circle plot of ΔU^* with the two parameters in figure 9. The cases for which $AR_C > 0.85$ were not considered as the definition of the capture angle (θ_C) becomes void, given that the major axis cannot be identified unambiguously for an ellipse whose aspect ratio is close to unity. One observation that can be made is that the number density of the circles in the plot is higher at lower θ_C values, which is consistent with our observation in figure 6 that the probability of bubble capture at lower θ_C is higher. The mechanism of reduction in the ring speed is similar to that in the case of bubble-circular vortex ring interactions as discussed in [10, 15]. The interacting bubble modulates the vorticity distribution of the ring leading to a reduction in its enstrophy. As the

convection speed is an integral measure of the vorticity, a reduction in the enstrophy also implies a reduction in the convection speed. The second observation we can make is that the circles in the plot appear larger on average at lower θ_C. This leads us to ask if there is any correlation between the final number of daughter bubbles (N_b), ring speed reduction (ΔU^*), and the capture angle (θ_C). To answer this, we average a reasonably large number of independent runs over different intervals of θ_C to make sense of the scatter observed in figure 9.

We thus plot the ring speed reduction (ΔU^*) with θ_C in figure 10. This plot shows a weak negative correlation between the ring speed reduction (ΔU^*) and the capture angle (θ_C), which means that a lower capture angle ($\theta_C \approx 0°$) causes a higher ring speed reduction ΔU^*. At different values of θ_C, the large variation is due to the lack of precise direct control over AR_C, which arises from the combined effect of the zigzag or helical trajectory of the rising bubble [19], the elliptic ring's axis switching and its 3D spatial deformation. This leads us to an immediate question about a possible correlation between the ring speed reduction (ΔU^*) and the number of daughter bubbles (N_b), which we investigate in figure 11. Although one could plot the variation of N_b over different experimental runs for different intervals of ΔU^*, we choose to plot the variation in ΔU^* for each value of N_b since N_b is better understood as a whole number. Here, we observe an increasing trend in the number of daughter bubbles (N_b) with the ring speed reduction (ΔU^*). This indicates that a higher number of daughter bubbles is produced when the ring undergoes a higher reduction in its speed. To summarise, in figure 11, we see a positive correlation between ΔU^* and N_b, while in figure 7, we observed a negative correlation between θ_C and N_b, and in figure 10, we observe a weak negative correlation between ΔU^* and θ_C. These correlations indicate that a lower capture angle ($\theta_C \approx 0°$) leads to a larger


Figure 6. Histogram of the capture angle (θ_C) computed using 55 independent experimental runs, in which only θ_C and AR_C are allowed to vary, showing a higher probability of capture at higher curvature regions ($\theta_C \approx 0°$) of the elliptic vortex ring. The schematic below the plot shows the position of the bubble during capture relative to the elliptic ring.

Figure 7. Variation of the number of daughter bubbles (N_b) with the capture angle (θ_C). Lower capture angles lead to a larger number of daughter bubbles. Although one could plot the variation of N_b over different experimental runs for different intervals of θ_C, we choose to plot the variation in θ_C for each value of N_b since N_b is better understood as whole number values. In this case, $We = 11$.
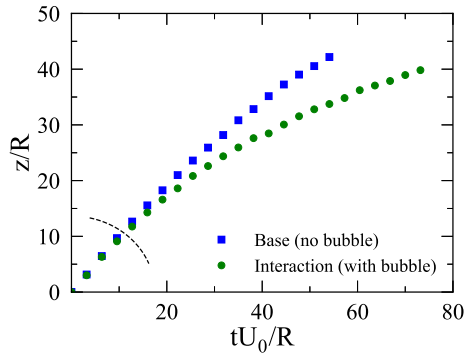
Figure 8. The vortex ring's vertical position (z/R) with time (tU_0/R) for the elliptic ring's ($AR_0 = 0.6$) base (no bubble) and interaction (with bubble) cases corresponding to $We = 11$. For the elliptic ring, $R = \sqrt{R_a R_b}$ is the radius of the area-equivalent circle. The interaction case shown in this plot is for $AR_C = 0.7$ and $\theta_C = 35°$. The slope of the curve gives the convection speed of the ring U_{base} and $U_{interaction}$, respectively, for the base and interaction cases. The reduction in the ring speed is computed as ΔU^* (%) = $100 \times (1 - U_{interaction}/U_{base})$ at a later time after capture ($tU_0/R \approx 29$ in this case; the bubble capture has occurred at $tU_0/R \approx 13$, marked by the dashed line in the plot).
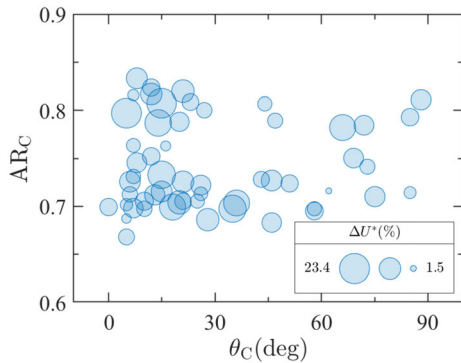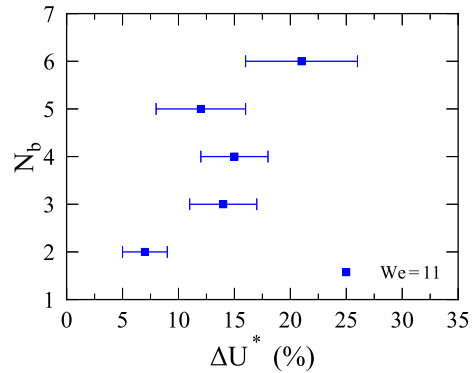

Figure 9. Circle plot of the ring speed reduction (ΔU^*) as a function of AR_C and θ_C. The diameters of the circles represent the magnitude of the ring speed reduction (ΔU^*). The large variation in the magnitude of ΔU^* is due to the lack of precise direct control over the parameters θ_C and AR_C during the capture, which arises from the combined effect of the zigzag or helical trajectory of the rising bubble, the elliptic ring's axis switching and its 3D spatial deformation.

number of daughter bubbles N_b and a higher reduction in convection speed ΔU^*.

From a first look at figure 11, one might be tempted to think that the reason for the larger number of daughter bubbles (N_b) at higher ring speed reductions (ΔU^*) is that the ring loses its kinetic energy to break the bubbles leading to an increase in the surface energy of the bubbles. However, the surface energy of the bubbles is an order of magnitude lower than the vortex ring's kinetic energy [8]. Therefore, the primary mechanism of the ring speed reduction is not the consumption of the ring's kinetic
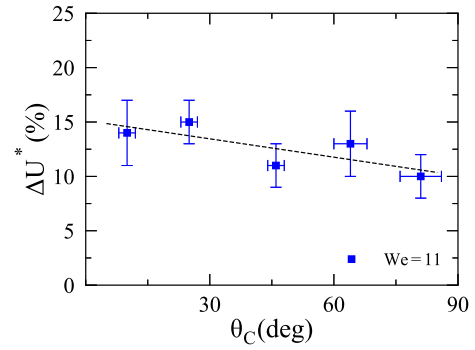
Figure 10. Variation of the ring speed reduction (ΔU^*) with the capture angle (θ_C). The large variation indicates the lack of precise direct control over the parameters θ_C and AR_C during the capture, which arises from the combined effect of the zigzag or helical trajectory of the rising bubble, the elliptic ring's axis switching and its 3D spatial deformation. In this case, $We = 11$.
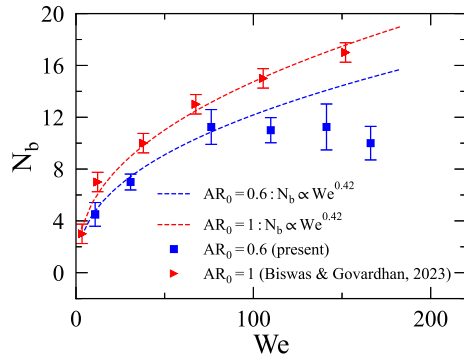

Figure 11. Variation of the number of daughter bubbles (N_b) with the ring speed reduction (ΔU^*). Although one could plot the variation of N_b over different experimental runs for different intervals of ΔU^*, we plot the variation in ΔU^* for each value of N_b since N_b is better understood as whole number values. In this case, $We = 11$.
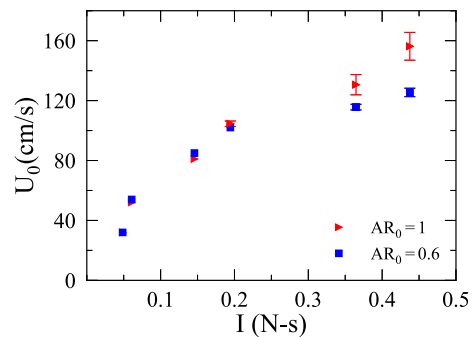
Figure 12. Variation of the ring's initial convection speed (U_0) with impulse (I) for different AR_0. At higher impulse values ($I \gtrsim 0.2$ N-s), the elliptic ring has a lower initial speed than the circular ring for the same impulse.

energy to break the bubble by increasing the surface energy but by a more complicated instability of the modified vortex core after bubble capture.

Figure 13. Variation of the number of daughter bubbles (N_b) with the Weber number (We). At higher We values ($We \gtrsim 100$), the elliptic ring ($AR_0 = 0.6$) gives rise to a smaller number of daughter bubbles than the circular ring ($AR_0 = 1$) [10]. Red dashed line represents $N_b \propto We^{0.42}$, as proposed in [10] for $AR_0 = 1$. Blue dashed line represents $N_b \propto We^{0.42}$ for the present data ($AR_0 = 0.6$). The number of broken bubbles N_b deviates from $We^{0.42}$ scaling beyond about $We \gtrsim 100$.

In this part of the study, the Weber number denoting the ratio of the ring's inertial effects to surface tension effects is fixed at $We = 11$. In the next subsection, we study the effect of the elliptic vortex ring's initial aspect ratio AR_0 over a range of Weber numbers and seek to compare the elliptic ring with the circular ring in terms of its interaction with the bubble.

3.2 *Effect of the elliptic ring's aspect ratio AR_0*

In §3.1, we examined the qualitative differences in the interaction of the elliptic and circular rings with a bubble. The ring's initial aspect ratio (AR_0) helps us characterise the two cases better. We consider $AR_0 = 0.6$ for the elliptic ring, and $AR_0 = 1$ denotes the circular ring. In these vortex ring-bubble interactions, the Weber number, defined in §1, is important [8]. In this part of the study, the capture angle for the elliptic ring would be an average value close to $\theta_C \approx 0°$, with distributions similar to figure 6. For the circular ring ($AR_0 = 1$), θ_C is not applicable, as the major and minor axes of a circle are identical. The ring's initial convection speed (U_0), computed just before the interaction begins, is controlled by varying the impulse (I) as discussed in §2. The ring's initial convection speed (U_0) is plotted with the impulse (I) in figure 12, where we observe that beyond $I \approx 0.2$ *N-s*, there is a reduced U_0 for the elliptic ring for the same impulse than for the circular ring. This is possibly due to the inherently unstable nature of the elliptic ring at high ring strengths corresponding to high U_0.

Regarding the bubble, we are interested to know how the relation of the number of daughter bubbles (N_b) with the Weber number (We) changes when AR_0 is changed. In the plot of N_b with We, shown in figure 13, we observe that the elliptic ring produces a lesser number of daughter bubbles

than the circular ring beyond $We \approx 100$. While for the circular ring ($AR_0 = 1$), N_b scales as $We^{0.42}$, as was observed by [10], for the elliptic ring ($AR_0 = 0.6$), N_b scales as $We^{0.42}$ only for low-to-moderate We. For $We \gtrsim 100$, the experimental data deviate from the $N_b \propto We^{0.42}$ scaling. The reason for this can be understood in terms of the ring's initial speed (U_0) shown in figure 12. For impulse values $I \gtrsim 0.2$ *N-s* corresponding to $We \gtrsim 100$, the initial speed of the elliptic ring is less than that of the circular ring. Thus, the elliptic ring is not strong enough to produce as many bubbles as a circular ring would produce. Therefore, at higher We, the circular vortex ring ($AR_0 = 1$) produces a greater number of daughter bubbles than the highly dynamic elliptic vortex ring ($AR_0 = 0.6$). Note that the Weber number in the reference [10] is defined using the ring's circulation instead of the initial convection speed (U_0). Therefore, in figure 13, the Weber number for their cases ($AR_0 = 1$) are recalculated based on our definition (§1) for consistency. The results in this section thus indicate that the vortex ring's aspect ratio AR_0 influences the scaling of the number of daughter bubbles N_b with the Weber number We.

The results of figure 13 could possibly have the following implications for a bubbly turbulent flow, where a local Weber number could represent the ratio of the strength of a hairpin vortex interacting with a bubble relative to the surface tension effects. We could think of the elliptic vortex ring as a representative of a hairpin vortex with higher spatial deformation, and the circular vortex ring as representing a hairpin vortex with lesser spatial deformation. In an interaction with a bubble, amongst the stronger vortices corresponding to a higher local We, the ones that exhibit more spatial deformation like the elliptic ring could produce a lesser number of broken bubbles than the less-deforming vortices like the circular vortex ring. On the other hand, weaker vortices interacting with the bubble might yield a similar number of broken bubbles, irrespective of the amount of their spatial deformation. However, one should note that, in a bubbly turbulent flow, it is possible that a single bubble interacts with multiple vortices and a single vortex could interact with multiple bubbles. Therefore, these results only give an insight into the physics in an idealised situation like the current bubble-elliptic ring configuration.

4. Conclusion

In this article, we have studied the effect of the vortex ring's aspect ratio (AR_0) on the interaction between an elliptic vortex ring and a bubble as an idealisation of the more complex bubbly turbulent flows. In the first part, we perform high-speed visualisations and detailed measurements of the interaction of an elliptic ring ($AR_0 = 0.6$) with the bubble. The capture angle (θ_C) is important in these

interactions. The bubble capture is more probable at lower capture angles ($\theta_C \approx 0°$), which implies that bubbles could more probably interact with the high-curvature regions of vortical structures in a bubbly turbulent boundary layer. Lower capture angles ($\theta_C \approx 0°$) lead to a larger number of daughter bubbles (N_b) and a higher reduction in the ring convection speed (ΔU^*). We also attempt to elucidate distinct bubble breakup mechanisms for the extreme values of the capture angle. Additionally, the bubble capture and elongation delay the ring's axis switching time period. In the second part of the study, we explore the effect of AR_0 on the parameters pertaining to the ring and bubble. At lower impulse, the initial convection speed of an elliptic ring is about the same as that of a circular ring. However, at higher impulses, the elliptic ring has a lower initial speed than the circular ring. The number of daughter bubbles is lower for the elliptic ring ($AR_0 = 0.6$) at higher Weber numbers, possibly due to the elliptic ring's lower initial speed than the circular ring. In a turbulent boundary layer, this could imply that, amongst the relatively stronger hairpin vortices, the less-deforming vortices (like the circular vortex ring) might produce a greater number of broken bubbles than the highly deformable ones (like the elliptic vortex ring). This work thus helps in gaining a better understanding of the complex bubbly turbulent boundary layer.

List of symbols

ϵ	Non-dimensional core radius
ρ	Water density
v	Water kinematic viscosity
θ_C	Capture angle
σ	Surface tension at water-air interface
$AR(t)$	Instantaneous aspect ratio of the elliptic vortex ring
AR_0	Vortex ring's initial aspect ratio
AR_C	Instantaneous aspect ratio of the elliptic vortex ring at bubble capture
D_b	Bubble diameter
D_n	Ring generator diameter
I	Impulse given to the piston
N_b	Final number of daughter bubbles
r_C	Dimensional core radius
R	Ring's effective radius
R_a	Semi-major axis of the ellipse
R_b	Semi-minor axis of the ellipse
t	Time
t_p	Axis-switch time period of the elliptic vortex ring
U_0	Vortex ring's initial convection speed
U	Vortex ring's convection speed
U_{base}	Ring's convection speed (base case)
$U_{interaction}$	Ring's convection speed (interaction case)
ΔU^*	Reduction in ring's convection speed
V_R	Volume ratio
We	Weber number
z	Ring's vertical position

References

[1] Elghobashi S 2019 Direct numerical simulation of turbulent flows laden with droplets or bubbles. *Annu. Rev. Fluid Mech.* 51: 217–244

[2] Steven Ceccio L 2010 Friction drag reduction of external flows with bubble and gas injection. *Annu. Rev. Fluid Mech.* 42: 183–203

[3] Varghese Mathai, Detlef Lohse and Chao Sun 2020 Bubbly and buoyant particle-laden turbulent flows. *Annu. Rev. Condens. Matt. Phys.* 11: 529–559

[4] Balachandar S and John Eaton K 2010 Turbulent dispersed multiphase flow. *Annu. Rev. Fluid Mech.* 42: 111–133

[5] Adrian R J, Meinhart C D and Tomkins C D 2000 Vortex organization in the outer region of the turbulent boundary layer. *J. Fluid Mech.* 422: 1–54

[6] Kazuyasu Sugiyama, Enrico Calzavarini and Detlef Lohse 2008 Microbubbly drag reduction in taylor-couette flow in the wavy vortex regime. *J. Fluid Mech.* 608: 21–41

[7] Sridhar G and Katz J 1999 Effect of entrained bubbles on the structure of vortex rings. *J. Fluid Mech.* 397: 171–202

[8] Narsing Jha K and Raghuraman Govardhan N 2015 Interaction of a vortex ring with a single bubble: Bubble and vorticity dynamics. *J. Fluid Mech.* 773: 460–497

[9] Subhajit Biswas and Raghuraman Govardhan N 2020 Effect of single and multiple bubbles on a thin vortex ring. *J. Flow Visual. Image Process.* 27: 1–27

[10] Subhajit Biswas and Raghuraman Govardhan N 2023 Vortex ring and bubble interaction: effects of bubble size on vorticity dynamics and bubble dynamics. *Phys. Fluids* 35(083328): 1–23

[11] Dhanak R M and de Bernardinis B 1981 The evolution of an elliptic vortex ring. *J. Fluid Mech.* 109: 189–216

[12] Clara O'Farrell and John Dabiri O 2014 Pinch-off of non-axisymmetric vortex rings. *J. Fluid Mech.* 740: 61–96

[13] Cheng M, Lou J and Lim T T 2016 Evolution of an elliptic vortex ring in a viscous fluid. *Phys. Fluids* 28: 037104

[14] Fazle Hussain and Hyder Husain S 1989 Elliptic jets. Part 1. Characteristics of unexcited and excited jets. *J. Fluid Mech.* 208: 257–320

[15] Subhajit Biswas and Raghuraman Govardhan N 2022 Interaction of a rigid buoyant sphere and a deforming bubble

with a vortex ring: The role of deformability. *Phys. Rev. Fluids* 7: 094302

[16] John Norbury 1973 A family of steady vortex rings. *J. Fluid Mech.* 57: 417–431

[17] Revuelta Antonio 2010 On the interaction of a bubble and a vortex ring at high reynolds numbers. *Eur. J. Mech.-B/Fluids* 29: 119-126

[18] Carlos Martínez-Bazán, Montañés L J and Juan Lasheras C 1999 On the breakup of an air bubble injected into a fully developed turbulent flow. Part 1. Breakup frequency. *J. Fluid Mech.* 401: 157–182

[19] Magnaudet Jacques and Eames Ian 2000 The motion of high-Reynolds-number bubbles in inhomogeneous flows. *Annu. Rev. Fluid Mech.* 32: 659–708